Solving Sensorless IPMSM Equations

Haomin Li, Babak Nahid-Mobarakeh, *Fellow, IEEE*, and Ali Emadi, *Fellow, IEEE*

***Abstract*—We show that the two equations of interior permanent magnet synchronous motors always satisfy four (speed, position) solution pairs, predetermining where sensorless algorithms will end up. With such finiteness, we see a silver lining in establishing theoretical basics for the open problem of startup with an unknown initial position. We reveal normal-reversal duality that demystifies the familiar binary behavior of sensorless field-oriented control (FOC) scheme with the genuine/specious pair, and devise a detection-quit mechanism to help FOC systems flee the specious pair using the knowledge of motor/generator mode. These two ingredients enable a tailored sensorless algorithm that can obviate the need for initial position detection.**

***Index Terms*—Initial position, interior permanent magnet synchronous motor (IPMSM), observer, sensorless.**

I. Introduction

WITHOUT costly, delicate encoders, sensorless interior permanent magnet synchronous motors (IPMSMs) are ideal for compactness and reliability [1], [2], [3]. The pair (speed, position) is typically obtained by trimming the motor model and fitting the resultant normal forms into a list of methodologies. Considering the mature classification in existing reviews [4], [5], [6], [7], [8], [9], [10] and the wealth of literature, we attempt to view numerous works through the lens of a crude binary breakdown, that is, seven fulfillments and two open problems. To this end, we invoke the ready criteria of a Texas Instruments (TI) product [11], which implies a nice, comprehensive summary of the current status and future challenges as follows:

(T1) No tuning parameter needed across various speed/loads.
(T2) No extra injection needed in full load zero speed startup.
(T3) Ample torque for heavy/full/overload applied at startup.
(T4) Position converges in the first startup cycle at any speed.
(T5) Superior, accurate speed and position estimation signal.
(T6) Completely stable speed reversals crossing zero-speed.
(T7) Stable operation for, including generator, all quadrants.
(T8) Startup with load subject to an unknown initial position.
(T9) Estimation at standstill for holding torque or stall restart.

Generally, (T1)–(T7) are basic criteria well fulfilled by the state-of-the-art (SOTA) sensorless solutions or observers, except for the tricky long-time ultralow/near-zero speed scenario due to the inevitable inverter irregularities, the biggest roadblock that hinders academic SOTAs or products. So commercial products, TI and Mitsubishi [12] for instance, only guarantee full torque below 1 Hz and 80% torque below 6 r/min, respectively. In contrast, (T8) and (T9) have not been well fulfilled, so that academic SOTAs mainly focus on cracking these two open problems rather than (T1)–(T7).

The persistent interest in (T9), namely zero-speed position estimation to reach full torque, has practical significance in scenarios where, e.g., a power drill holds a screw, or a bicycle stalls on a slope, or a crane lifts objects. Thus, (T9) is essential for all leading products, examples include STMicroelectronics ZeST [13], TI FAST, and Mitsubishi. The demand for (T9) leads to three typical research lines. The high-frequency signal injection line is dedicated to 0 r/min position estimation and performs the best zero-speed full torque delivery [5]. The flux-based line has the advantage of independence from speed. To name but a few SOTAs, both the incipient active flux proposals [14], [15] and recent designs [16], [17] exhibit successful full load capability at 1 r/min ultralow-speed or 0 r/min. Several SOTAs along the current derivative line also enable excellent zero-speed full-load performance [18], [19].

However, existing knowledge and theory for the other open problem (T8) is incomplete. The only fact we know for sure so far is that sensorless algorithms eventually end up converging to a (speed, position) pair need not match up the real-world, and that sensorless IPMSM systems fed by an erroneous pair may crash quickly. Starting out from this basic fact, it follows that fulfilling startup with an unknown initial position amounts to a stepwise procedure of getting through the following three problems.

(P1) List out all the possible pairs, one real and the rest being erroneous, that sensorless algorithms end up with.
(P2) Pick out the specious pairs that can help manage control systems to buy time for self-check, avoiding utter crash.
(P3) Figure out how to let the deceived control system realize and flee specious pairs to get back to the real-world pair.

The first contribution is the answers to (P1)–(P3) as follows:

- The IPMSM dynamics fits in a special structure and hence always have four solutions, answering (P1) and yielding a tailored sensorless algorithm that only covers (T1)–(T7).
- The normal-reversal duality concept, answering (P2) and identifying a specious pair that can manage to keep sensorless control systems from crash, though imperfectly.
- A quit mechanism based on normal-reversal duality and the knowledge of motor/generator mode, answering (P3) and upgrading the primitive algorithm to cover (T1)–(T8).

Manuscript received 15 December 2023; revised 17 March 2024; accepted 23 April 2024. Date of publication 24 May 2024; date of current version 4 September 2024. This work was supported by the Canada Research Chair in Transportation Electrification and Smart Mobility and MITACS. Recommended for publication by Associate Editor L. V. Iyer. *(Corresponding author: Haomin Li.)*

The authors are with the McMaster Automotive Resource Centre, McMaster University, Hamilton, ON L8P 0A6, Canada (e-mail: lih259@mcmaster.ca; babak.nahid@mcmaster.ca; emadi@mcmaster.ca).

Color versions of one or more figures in this article are available at https://doi.org/10.1109/TPEL.2024.3404937.
Digital Object Identifier 10.1109/TPEL.2024.3404937

The second contribution is that the algorithm, arising from (P1), keeps the IPMSM model fully intact and hence is tailored for IPMSMs, not compromising with any ready methodology. The biggest drawback of this algorithm, occurred unexpectedly in experiments as opposed to simulations, is its severe sensitivity to the variation of rotor flux parameter.

II. Main Results

In the $\alpha\beta$ frame, u_α, u_β, and i_α, i_β are the stator voltages and currents. ψ_m is the permanent magnet flux. R is the stator resistance. $L_0 = (L_d + L_q)/2$ and $L_1 = (L_d - L_q)/2$, where L_d and L_q are the dq-axes inductances. ω and θ are the electrical speed and position. T_e and T_L are the electromagnetic torque and load. i_d and i_q are dq-axes currents. $\hat{\omega}, \hat{\theta}, \hat{T}_e, \hat{i_d}, \hat{i_q}$ denote estimates and $\tilde{\theta} = \theta - \hat{\theta}$ is the position error. ω^*, i_d^*, i_q^* denote references.

A. Solving Sensorless IPMSM Equations

We attempt to answer (P1) with a byproduct in [20] and the metaphor of fate versus fortune. We consider a special system of nonlinear equations, which comprises two unknowns $(\hat{\omega}, \hat{\theta})$ and seven arbitrary coefficients $B_1, B_2, B_3, B_4, B_5, B_6, B_7$

$$B_1 \cos 2\hat{\theta} + B_2 \sin 2\hat{\theta} - B_3\hat{\omega} \sin 2\hat{\theta} + B_4\hat{\omega} \cos 2\hat{\theta} - B_5\hat{\omega} \sin \hat{\theta} + B_6 = 0 \tag{1a}$$

$$B_1 \sin 2\hat{\theta} - B_2 \cos 2\hat{\theta} + B_3\hat{\omega} \cos 2\hat{\theta} + B_4\hat{\omega} \sin 2\hat{\theta} + B_5\hat{\omega} \cos \hat{\theta} + B_7 = 0. \tag{1b}$$

Its exact solutions could be formulated, and the number of solutions is four [20], an independent constant regardless of arbitrary $B_1, B_2, B_3, B_4, B_5, B_6, B_7$ values. On the other hand, the values of its four solutions, as denoted as follows,

$$(\hat{\omega}_1, \hat{\theta}_1), \quad (\hat{\omega}_2, \hat{\theta}_2), \quad (\hat{\omega}_3, \hat{\theta}_3), \quad (\hat{\omega}_4, \hat{\theta}_4) \tag{2}$$

are highly irregular due to the intricate dependence on arbitrary $B_1, B_2, B_3, B_4, B_5, B_6, B_7$ values, moreover, the nature of (2) is indeterminate, being all real, or all complex, or in-between.

Turning back to (P1), the IPMSM electrical dynamics is

$$u_\alpha = Ri_\alpha + L_0\dot{i_\alpha} + L_1\dot{i_\alpha} \cos 2\theta + L_1\dot{i_\beta} \sin 2\theta - 2L_1 i_\alpha \omega \sin 2\theta + 2L_1 i_\beta \omega \cos 2\theta - \psi_m \omega \sin \theta \tag{3a}$$

$$u_\beta = Ri_\beta + L_0\dot{i_\beta} + L_1\dot{i_\alpha} \sin 2\theta - L_1\dot{i_\beta} \cos 2\theta + 2L_1 i_\alpha \omega \cos 2\theta + 2L_1 i_\beta \omega \sin 2\theta + \psi_m \omega \cos \theta \tag{3b}$$

where ψ_m, R, L_0, L_1, and $i_\alpha, i_\beta, u_\alpha, u_\beta$ are known, but ω, θ are unknown in sensorless terms. If we link its seven random coefficients $L_1\dot{i_\alpha}, L_1\dot{i_\beta}, 2L_1 i_\alpha, 2L_1 i_\beta, \psi_m, L_0\dot{i_\alpha} + Ri_\alpha - u_\alpha, L_0\dot{i_\beta} + Ri_\beta - u_\beta$ to $B_1, B_2, B_3, B_4, B_5, B_6, B_7$, it is clear (3) fits exactly in the form of (1), implying the fate of the electrical dynamics is predetermined and has to always satisfy four (speed, position) pairs impossible to tell apart. Besides, such constant four never changes despite varying/uncertain/erroneous ψ_m, R, L_0, L_1 parameters, or injecting high-frequency signals in $u_\alpha, u_\beta, i_\alpha, i_\beta$, or sensor drift/noise/failures, or u_α, u_β mismatches of inverter irregularities, or filtered $\dot{i_\alpha}$, $\dot{i_\beta}$, or motor fault/malfunctions, etc.

Using a new letter τ, we pack up (3a) and (3b) as $\tau_\alpha(\omega, \theta) = \tau_\beta(\omega, \theta) = 0$, respectively, to present (3) in a compact form

$$\tau(\omega, \theta) = 0. \tag{4}$$

Looking on the bright side, four has capped the worst-case scenario, so indistinguishability cannot be any worse. Despite this destined constant, the electrical dynamics comes with two inherent fortunes, namely a real-world rotor and the sinusoidal nature, so that the four solutions of (4) exhibit a more refined characterization in contrast to the crude characterization of (2), paving the way for the development of a sensorless algorithm.

In contrast to the indefinite nature of (2), the existence of a real-world (ω, θ) narrows the feasibility of the four solutions of (4) down to either of the two cases [20, Prop. 14]

$$(\omega, \theta), \quad (\omega', \theta'), \quad (\omega'_c, \theta'_c), \quad (\overline{\omega'_c}, \overline{\theta'_c}) \tag{5a}$$

$$(\omega, \theta), \quad (\omega', \theta'), \quad (\omega'_1, \theta'_1), \quad (\omega'_2, \theta'_2) \tag{5b}$$

and particularly, solving (4) given a zero-speed rotor yields

$$(0, \theta), \quad (0, \theta + \pi), \quad (\omega'_{c0}, \theta'_{c0}), \quad (\overline{\omega'_{c0}}, \overline{\theta'_{c0}}) \tag{6a}$$

$$(0, \theta), \quad (0, \theta + \pi), \quad (\omega'_{10}, \theta'_{10}), \quad (\omega'_{20}, \theta'_{20}) \tag{6b}$$

where the case (5a) implies two real solutions $(\omega, \theta), (\omega', \theta')$ and two complex conjugate solutions $(\omega'_c, \theta'_c), (\overline{\omega'_c}, \overline{\theta'_c})$, whereas the second case (5b) implies all four solutions are real. Due to the fact (2) depends on the random $B_1, B_2, B_3, B_4, B_5, B_6, B_7$ coefficients intricately, the three specious solutions are random as well, depending on both all the coefficients of (4) and (ω, θ).

Up to now, the characterization of two feasible cases in (5) is the farthest theoretical end we can reach with rigor. However, (5) does not offer any knowledge about the difference amongst the solutions to tell apart at least (ω, θ) and (ω', θ'). Thus, we have to explore how the sinusoidal nature, the second fortune, can further enhance the characterization of four solutions based on the refined characterization given in (5). We accept that the use of such sinusoidal fortune may be disliked in [20, Sec. IV-E], which exhibits pragmatic intuition, assumption, at the cost of losing rigor and implying flaws, completely out of tune with the rest of the contents of [20]. In fact, it is driven by a wish to see the rough difference between (ω', θ') and (ω, θ), and by the idea that the more knowledge, the more chance we can make a difference, or otherwise we have to stop at (5) and cannot advance to enhance theoretic basics for (T8).

To elaborate, $i_\alpha = i_d \cos\theta - i_q \sin\theta, i_\beta = i_d \sin\theta + i_q \cos\theta$, and $\dot{i_\alpha} = -i_d\omega \sin\theta - i_q\omega \cos\theta, \dot{i_\beta} = i_d\omega \cos\theta - i_q\omega \sin\theta$, assuming i_d, i_q constants, imply i_α, i_β and $\dot{i_\alpha}$, $\dot{i_\beta}$ are sinusoidal whose orbit is only a circle but not the entire plane. Thus, the coefficients of (4) are sinusoidal and correlated with the real-world (ω, θ), taking up only a tiny part of the entire world the arbitrary and irregular $B_1, B_2, B_3, B_4, B_5, B_6, B_7$ coefficients of (1) live in. It follows that the solutions in (5) are much less arbitrary and less irregular than the solutions presented in (2).

Such significantly drastic coefficient restriction significantly slashes arbitrariness and irregularity, further narrows the two feasible cases in (5) down to only one case (5a), resulting in

$$(\omega', \theta') \approx (-\omega, \theta + \pi) \tag{7}$$

which grips the primary difference between (ω, θ) and (ω', θ'), telling how (ω', θ') looks like in terms of the real-world (ω, θ).

It is important to interpret (7) as carrying extra knowledge. First, $\omega' \approx -\omega$ tells the primary difference between ω' and ω is a negative sign, which should never be viewed as $|\omega'| = |\omega|$. Second, $\theta' \approx \theta + \pi$ tells the primary difference between θ' and θ is an offset that fluctuates around π. So equality never occurs in (7), and the incipient interpretation in [20, Sec. IV-E] is incorrect and lacks maturity. In fact, (7) can be viewed as the more an IPMSM differs from a surface-mounted motor, or the higher the saliency L_q/L_d, the more (ω', θ') deviates from the prediction $(-\omega, \theta + \pi)$, preserving only primary differences.

Since solving (4) amounts to a minimization process in (8), a primitive sensorless algorithm can be developed as follows:

$$(\hat{\omega}, \hat{\theta}) = \arg\min\ {\tau_\alpha}^2(\hat{\omega}, \hat{\theta}) + {\tau_\beta}^2(\hat{\omega}, \hat{\theta}), \quad 0 \le \theta < 2\pi \tag{8}$$

which exhibits the following two basic features.

- By (5a), the estimated pair $(\hat{\omega}, \hat{\theta})$ converges either to the real-world (ω, θ) or otherwise to (ω', θ'), since the other two complex pairs do not exist in the real world.
- By (7), (ω, θ) and (ω', θ') are very far apart at any speed (slightly disagrees with the incipient gist in [20, Sec. V-A] that lacks maturity), implying that startup under unknown initial position is the only cause of converging to (ω', θ').

As analyzed above and verified later in copious simulations and experiments, the only cause the primitive solver (8) ends up at (ω', θ') is heavy load startup with unknown large initial position errors, or otherwise (8) itself is fully adequate to meet (T1)–(T7). Hence, for applications without the unknown large initial position error problem, Sections II-B and II-C, which is merely to upgrade (8) to meet (T8), can be neglected.

B. Sensorless Normal-Reversal Duality

We answer (P2) by showing the specious pair (ω', θ') does not cause an utter crash, but deceives controllers into thinking everything works fine, resulting in normal-reversal duality. To demystify, it characterizes two states sensorless FOC schemes can function stably: a genuine stable state using (ω, θ) for Park transform, and an imperfect reverse state using (ω', θ'). The key to analyze why using (ω', θ') for Park transform can still manage FOC systems is $\theta' \approx \theta + \pi$, as converting (3) with θ' directly leads to a form too lengthy and complicated to analyze.

The classical FOC scheme, of course taking for granted that the real-world rotor position θ is used for Park transform, is shown in Fig. 1 and expressed as follows:

$$u_d - L_q\omega i_q = L_d\dot{i_d} + Ri_d - L_q\omega i_q \tag{9a}$$

$$u_q + L_d\omega i_d + \psi_m\omega = L_q\dot{i_q} + Ri_q + L_d\omega i_d + \psi_m\omega \tag{9b}$$

where the left-hand side of (9a) and (9b) are the total control outputs, comprising decoupling terms and the outputs u_d and u_q

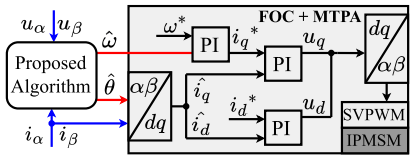

Fig. 1. Classical sensorless FOC diagram.

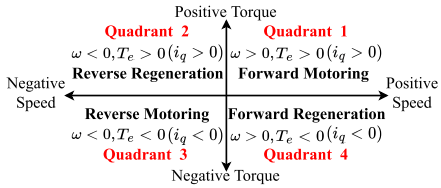

Fig. 2. Motor/generator mode of four quadrants.

of two PI current controllers. Based on the simple linear structure $u_d = L_d\dot{i_d} + Ri_d$ and $u_q = L_q\dot{i_q} + Ri_q$ in the normal sensorless state, the parameters of dq current controllers can be finalized, so that u_d regulates i_d well, and u_q regulates i_q well.

Applying Park transform with $\theta + \pi$ and keeping the classical controller design policy of (9) unchanged, we convert (3) into

$$u'_d - L_q\omega' i'_q = L_d\dot{i'_d} + Ri'_d - L_q\omega i'_q \tag{10a}$$

$$u'_q + L_d\omega' i'_d + \psi_m\omega' = L_q\dot{i'_q} + Ri'_q + L_d\omega i'_d - \psi_m\omega \tag{10b}$$

where i_α, i_β become i'_d, i'_q. u_α, u_β become the left-hand side, which comprises decoupling terms and the outputs u'_d and u'_q of two PI current controllers. Considering $\psi_m\omega' \approx -\psi_m\omega$ and neglecting the small terms $L_d\omega' i'_d$ and $L_d\omega i'_d$, (10b) becomes $u'_q \approx L_q\dot{i'_q} + Ri'_q$, the same linear system as $u_q = L_q\dot{i_q} + Ri_q$, so the originally finalized q-axis PI controller can regulate i'_q well. While (10a) exhibits a linear structure with an additional disturbance, namely $u'_d = L_d\dot{i'_d} + Ri'_d + L_q(\omega' - \omega)i'_q$, so the originally finalized d-axis controller, being PI type, can still regulate i'_d, but may not as good as how it regulates i_d based on the clean linear system structure $u_d = L_d\dot{i_d} + Ri_d$.

Regulating i'_q through the lens of $\theta + \pi$-based coordinate is equivalent to regulating i_q through the lens of the well-known θ-based coordinate. Moreover, i'_q differs from i_q up to a sign since $i'_q \approx -i_\alpha \sin(\theta + \pi) + i_\beta \cos(\theta + \pi) = -i_q$.

It is important to note that we merely study how the original FOC system behaves if the estimated $(\hat{\omega}, \hat{\theta})$ of (8) converges to $(-\omega, \theta + \pi)$, a best-case scenario capturing primary features for the sake of analysis. However, $(\hat{\omega}, \hat{\theta})$ indeed converges to (ω', θ'), which may deviate away from $(-\omega, \theta + \pi)$ a lot, e.g., if the saliency is large, and the reverse state control performance based on (ω', θ') may deteriorate significantly and not as what the above analysis predicts. Hence, a quit mechanism is needed, both to detect whether the algorithm (8) gets trapped at (ω', θ') and help get back to (ω, θ). The key to the quit mechanism is the knowledge of motor/generator mode, as shown in Fig. 2.

To sum up, startup with unknown initial position may cause the algorithm soon converge to (ω', θ'), getting in the reverse sensorless state. Despite possible flaws and glitches, the FOC

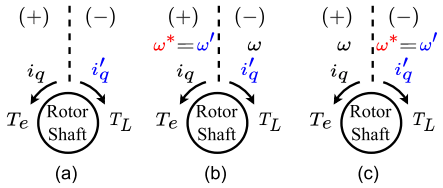

Fig. 3. Actual, observed, and expected modes.

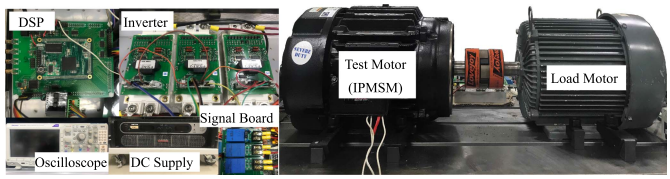

Fig. 4. Description of the IPMSM drive test setup.

system that takes (ω, θ) based transform for granted can still manage imperfectly with (ω', θ') based transform, buying time for the quit mechanism to detect and interfere to force the FOC system back to the normal sensorless state. Thus, in terms of how soon such quit mechanism acts, which can be flexibly set by a timeout whose counting begins with the algorithm launch, we suggest the earlier the better, before the situation deteriorates to an extent much more than the FOC system can manage.

C. Detection-Quit Mechanism

This section is to make the article self-contained without the need to reach [20, Sec. V-A], which answers (P3).

Without loss of generality, counterclockwise rotation/torque are assigned the sign "+," and clockwise rotation/torque the sign "−." Since it is the actual q-axis current i_q that generates electromagnetic torque to resist T_L, the sign of i'_q is the same as T_L, as Fig. 3(a) shows. The speed controller regulates ω' to track the reference ω^* since (ω', θ') traps the algorithm, so the sign of ω' matches the sign of ω^*, and the sign of ω opposites the sign of ω^* as $\omega \approx -\omega'$. The two resultant operations are shown in Fig. 3(b) and (c), which are detailed as follows.

Actual mode $i_q^*\omega^*$	Observed mode $i'_q\omega'$	Command mode ω^*T_L	Refer to
Generator (+)(−)	Generator (−)(+)	Motor (+)(−)	Fig. 3(b)
Motor (+)(+)	Motor (−)(−)	Generator (−)(−)	Fig. 3(c)

It shows the following three classes of knowledge of motor/generator mode.

- Real-world motor/generator mode, which is unknown to an algorithm, implied by the +/− sign of $i_q\omega$, respectively.
- Observed motor/generator mode, which is available to an algorithm, implied by the +/− sign of $i'_q\omega'$, respectively.
- Expected motor/generator mode, which is available to an algorithm, implied by the −/+ sign of ω^*T_L, respectively.

Thus, the real-world and the observed motor/generator mode always coincide, implying motor/generator modes are reliable in the sensorless setting, regardless of IPMSMs operating with the real-world (ω, θ) or cheated by the specious (ω', θ').

Once algorithms get trapped, a detectable mismatch between the command and observed motor/generator mode will happen. Hence, the primitive algorithm (8) can be upgraded as follows.

Solver: Implement (8) to get a feasible pair $(\hat{\omega}, \hat{\theta})$.

Detection & Correction: Activate a timer at startup, if the sign of $\hat{i_q}\hat{\omega}$ indicating the observed mode disagrees with the command mode at timeout, then execute $\hat{\omega} \leftarrow -\hat{\omega}$, $\hat{\theta} \leftarrow \hat{\theta} - \pi$.

Although (8) can be implemented by any numerical method, in later simulations and experiments it is only implemented in the simplest way, namely the steepest gradient descent method.

III. Performance Evaluation

The parameters are $R = 0.4\,\Omega$, $L_d = 11$ mH, $L_q = 14.3$ mH, and $\psi_m = 0.343$ wb, the rated torque 23.6 Nm, and the pole pair number 5. The rated speed is 900 r/min. The dc-link voltage is 300 V. The IPMSM is controlled by TMS320F28377D and driven by a three-phase voltage source inverter with Infineon IGBTs, as shown in Fig. 4. The control frequency is 10 kHz, and the dead-time is 2 μs.

In all simulations and experiments the common settings are as follows.

- The gradient step size is set as 0.1, which is not optimal.
- A load torque step is applied at $t = 0$, the startup instant.
- A speed step command is given at $t = 0$ for self startup.

Experiments are designed to benchmark (T1)–(T8), including the following:

- To benchmark (T3), 80% and 110% step loads are applied at startup to result in 150% torque delivery intentionally.
- To benchmark (T6) and (T7) three fast reversals are tested
  a) Quadrant 1 to 2, reversing only the speed direction.
  b) Quadrant 1 to 4, reversing only the torque direction.
  c) Quadrant 1 to 3, with both speed and torque reversed.
- To benchmark (T8), four initial error setups are performed
  a) Small $\hat{\theta}(0)$ error, not triggering detection/correction.
  b) Small $\theta(0)$ offset, not triggering detection/correction.
  c) Large $\hat{\theta}(0)$ error, able to trigger detection/correction.
  d) Large $\theta(0)$ offset, able to trigger detection/correction.

We tested the algorithm with the ready TI criteria (T1)–(T8) and summarized the performance evaluation of all simulations and experiments in Table I. Experimental results meet simulation expectations, for example, a large unknown initial position offset is the only cause that can activate the quit mechanism.

We noticed three evident drawbacks of our algorithm when put in experiments. First, speed estimate is sensitive to the flux parameter ψ_m, an unexpected severe drawback violating even the most basic criterion (T5), for which we suggest calibration. Second, the low-speed performance degrades severely, and the motor stalled below 10 r/min in experiments, partly because the dead-time devoured most voltage and left nothing to it. Third, we did not conduct tests for (T9), partly because telling apart $(0, \theta), (0, \theta + \pi)$ in (6) is difficult without extra knowledge.

Experiments and simulations, without voltage compensation and filter techniques, are not optimal for objective evaluation.

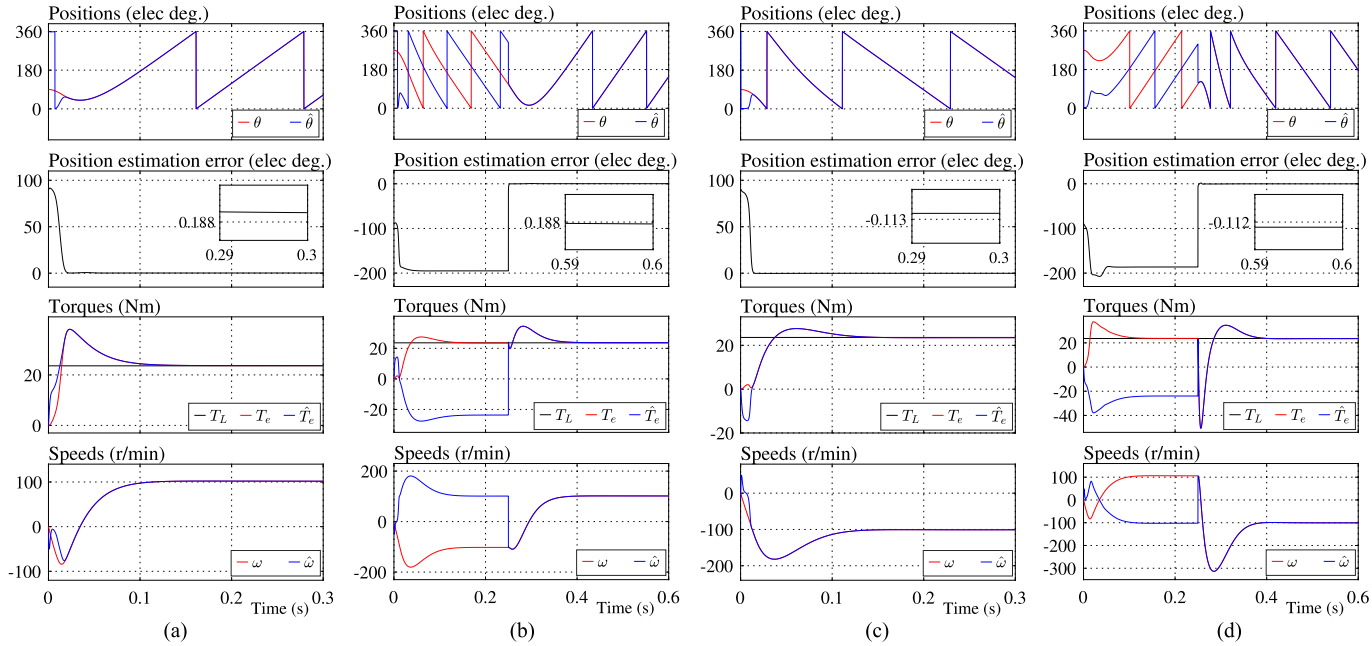

Fig. 5. (a) Full load startup with an initial $+90^\circ$ position error, $+100$ r/min. (b) Full load startup with an initial -90° position error, $+100$ r/min. (c) Full load startup with an initial $+90^\circ$ position error, -100 r/min. (d) Full load startup with an initial -90° position error, -100 r/min.

TABLE I
PERFORMANCE EVALUATION

Term	Please refer to figures	
	Simulations	Experiments
(T1) $\surd$	A numerical implementation of (8)	
(T2) $\surd$	All figures	Fig. 9a, Fig. 10b
(T3) $\surd$	All figures	Fig. 9a, Fig. 10b
(T4) $\surd$	All figures	Fig. 8a–Fig. 14b
(T5) $\surd$	All figures	All figures
(T6) $\surd$	All figures	Fig. 8c–Fig. 10b, Fig. 11b–Fig. 13a
(T7) $\surd$	All figures	Fig. 9a–Fig. 10c, Fig. 11b–Fig. 13a
(T8) $\surd$	Fig. 5a–Fig. 5d, Fig. 7c	Fig. 11b–Fig. 14a
(T9) $\times$	Fig. 7a–Fig. 7d	Fig. 14b

We suggest extra compensation for inverter irregularities and dead-time effects to max out the simulation feasibility.

A. Simulations

Figs. 5(a)–(d) show startup of ± 100 r/min full load speed step responses, with large unknown initial position offsets to verify the correction mechanism. To this end, the timeout of the timer was set to 0.25 s, and the other setups, with $\hat{\theta}(0) = 0$, were as follows.

1) The exact command was forward motoring at $+100$ r/min.
   a) Fig. 5(a) shows, with an unknown initial offset $\theta(0) = +90^\circ$, the mode was observed as Quadrant 1, which matched the command and did not trigger correction.
   b) Fig. 5(b) shows an unknown $\theta(0) = -90^\circ$ initial offset led to the observed mode being forward regeneration as against the command mode, triggering correction.
2) The exact command was -100 r/min reverse regeneration.
   a) Fig. 5(c) shows, with an unknown initial offset $\theta(0) = +90^\circ$, the mode was observed as Quadrant 2, which matched the command and did not trigger correction.
   b) Fig. 5(d) shows an unknown $\theta(0) = -90^\circ$ initial offset resulted in the observed mode being reverse motoring as against the command mode, triggering correction.

Figs. 6(a) and (b) show speed step responses at, respectively, 100 r/min and 10 r/min as well as, respectively, ± 100 r/min and ± 10 r/min fast reversal under full load. The load step applied at startup caused spin reversal and fast shift into Quadrant 2.

Fig. 6(c) shows full load step applied at steady-state 100 r/min.

Fig. 6(d) shows full load step applied at 10 r/min, causing fast shift to Quadrant 2, spin reversal, and recovery to Quadrant 1.

Figs. 7(a)–(d) show repeated tests at near zero speeds, where inverter irregularities became unignorable.

Fig. 7(a) shows 1 r/min speed step response with full load and ± 1 r/min fast reversal. The load step applied at startup caused drastic spin reversal, fast shift to Quadrant 2, and fast recovery.

Fig. 7(b) shows full load step applied at a steady speed 1 r/min.

Fig. 7(c) shows startup under full load step, with the command being 1 r/min in Quadrant 1. An unknown $\theta(0) = +120^\circ$ initial offset caused the observed mode being regeneration in Quadrant 2 as against the command, thus triggering correction.

Fig. 7(d) shows the speed step response under 0.1 r/min command with a full load step applied at startup. The position estimation error at 0.1 r/min was significant without compensation.

It follows that experiments would be worse than simulations.

B. Experiments

Fig. 8(a) shows a 100% load step applied at steady 300 r/min.

Fig. 8(b) shows a 110% load step was applied when the motor was running steadily at 100 r/min, resulting in a transient stall.

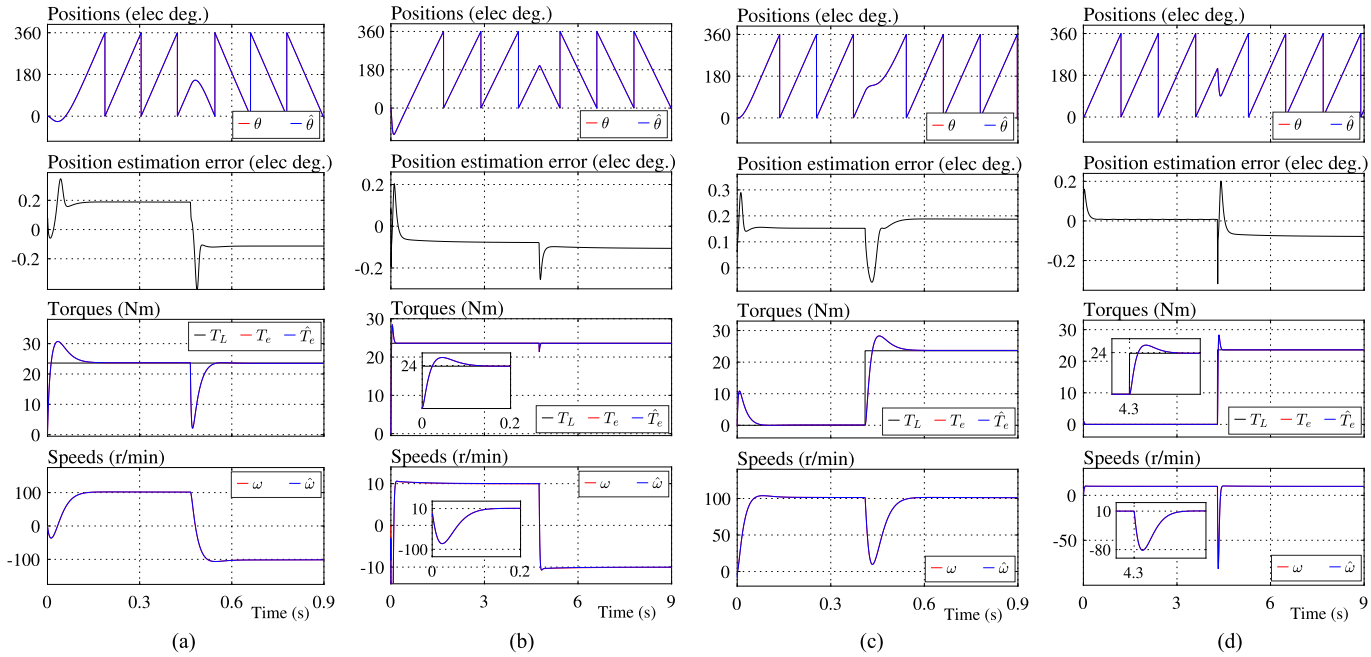

Fig. 6. (a) Full load 100 r/min startup and fast ±100 r/min speed reversal. (b) Full load 10 r/min startup and fast ±10 r/min speed reversal. (c) Startup and full load step applied to a steady speed 100 r/min. (d) Startup and full load step applied to a steady speed 10 r/min.

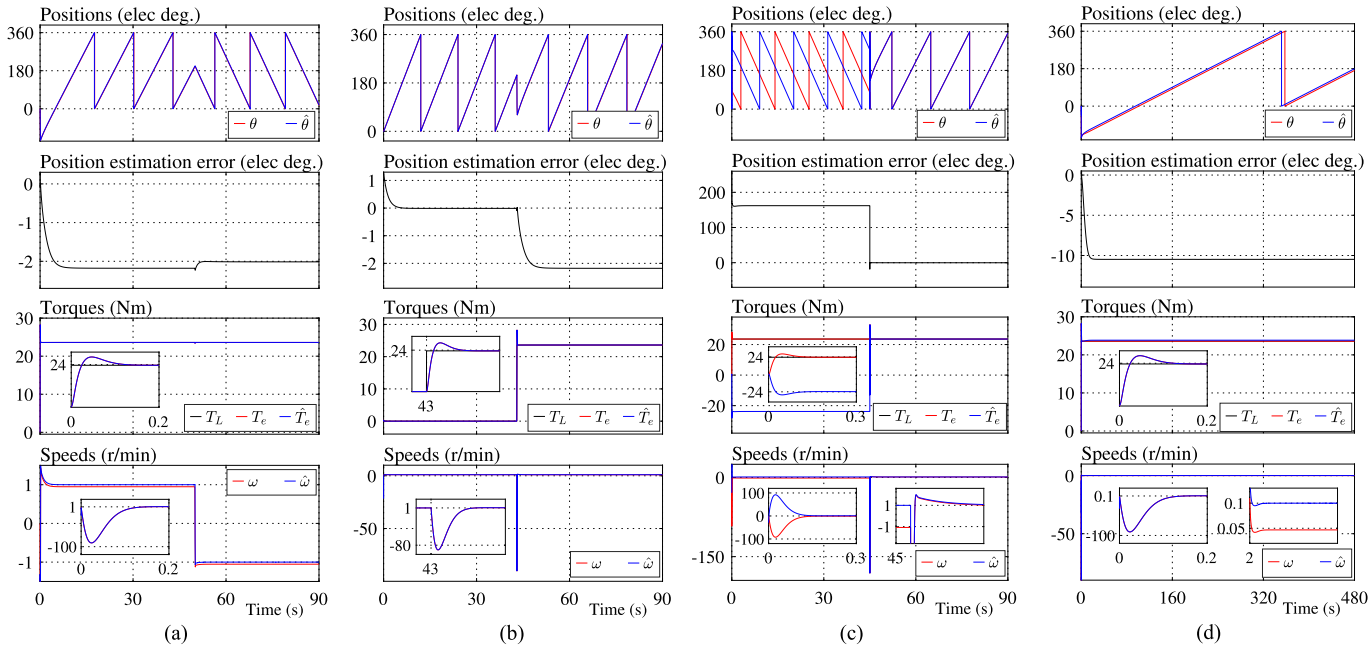

Fig. 7. (a) Full load startup at 1 r/min and fast speed reversal at ±1 r/min. (b) Drastic spin reversal near zero due to full load step at 1 r/min. (c) Full load startup under an +120° initial position offset, 1 r/min. (d) Speed step response with a full load step at startup, 0.1 r/min.

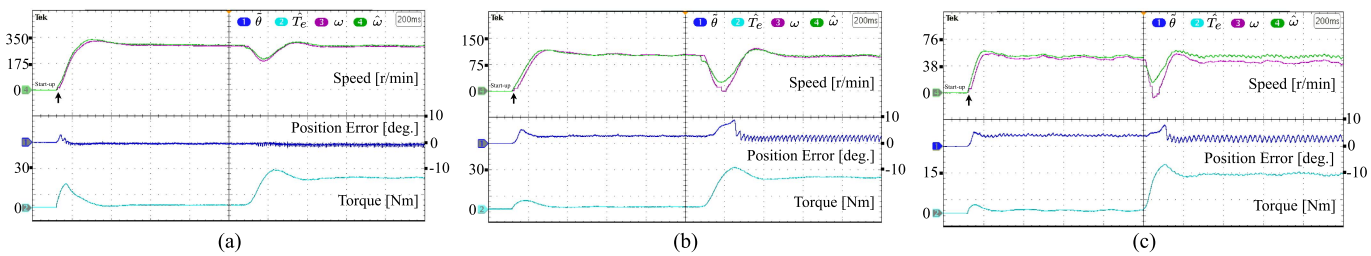

Fig. 8. (a) 100% load step applied at 300 r/min. (b) 110% load step applied at 100 r/min. (c) 50% load step applied at 50 r/min.

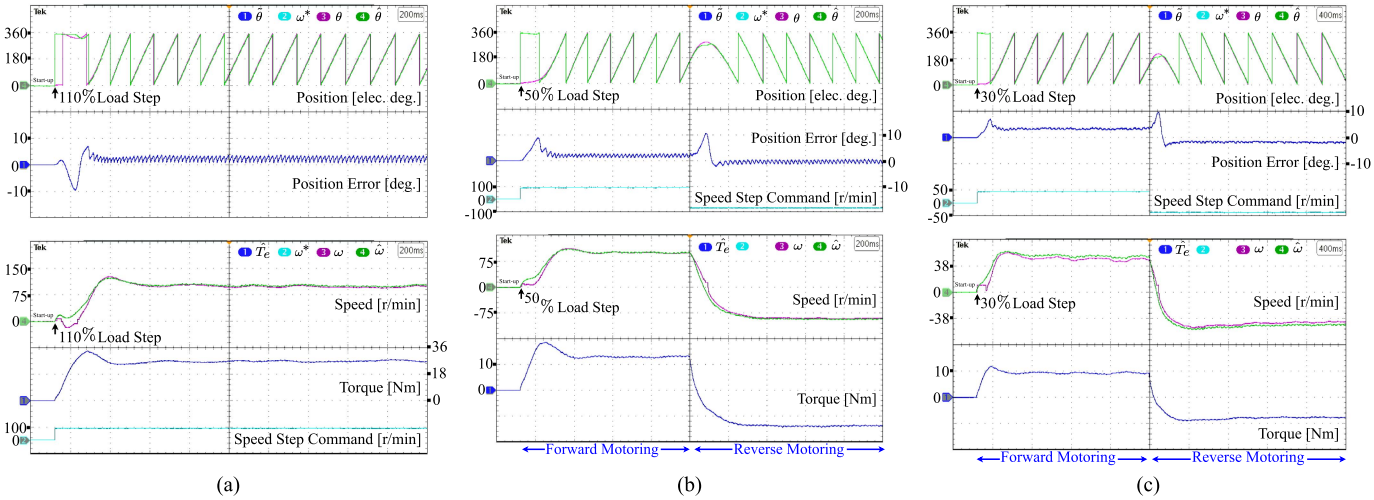

Fig. 9. (a) Speed step response of 100 r/min command, with a 110% load step applied at startup. (b) Fast ±100 r/min speed step responses and quadrant shift to Quadrant 3, with a 50% startup load step. (c) Fast ±50 r/min speed step responses and quadrant shift to Quadrant 3, with a 30% startup load step.

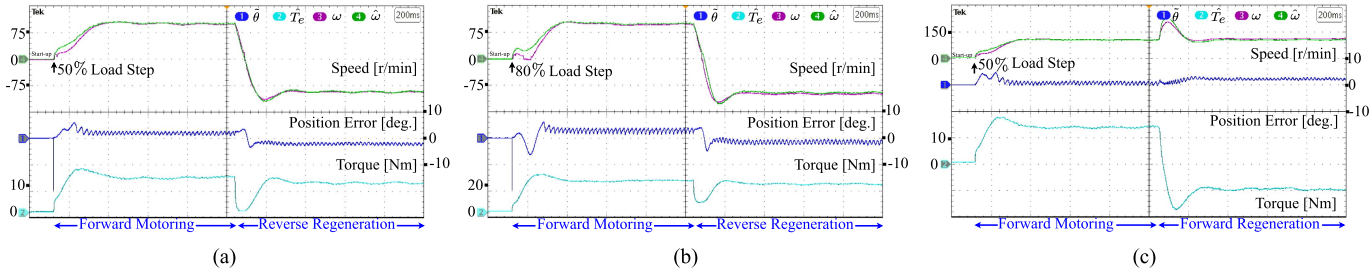

Fig. 10. (a) Speed step response at 100 r/min with a 50% startup load step, fast ±100 r/min speed step reversal, and quadrant shift to Quadrant 2. (b) Speed step response at 100 r/min with a 80% startup load step, fast ±100 r/min speed step reversal, and quadrant shift to Quadrant 2. (c) Speed step response at 100 r/min with a 50% load step applied at startup, switch of load step direction, and quadrant shift to Quadrant 4.

Fig. 8(c) shows a 50% load step applied at steady-state 50 r/min, causing a bigger speed error. This implied the severe low-speed degradation of our algorithm without inverter compensation.

Fig. 9(a) shows the speed step response at 100 r/min, with a 110% load step applied at the startup moment. The load motor was stronger than the test motor, causing a slight startup reversal.

The quadrant tests in Figs. 9(b) and (c) were challenging.

Fig. 9(b) shows ±100 r/min step responses under 50% startup load step, and tough quadrant transition from forward motoring mode (Quadrant 1) into reverse motoring mode (Quadrant 3), after changing the direction of both load and speed command.

Fig. 9(c) shows ±50 r/min step responses under 30% startup load step, and tough quadrant transition from forward motoring mode (Quadrant 1) into reverse motoring mode (Quadrant 3), changing simultaneously the direction of speed command and load. Speed estimation error was bigger compared with Fig. 9(b).

Fig. 10(a) shows a 100 r/min step response with a 50% startup load step, fast ±100 r/min spin reversal and quadrant shift from forward motoring mode (Quadrant 1) to reverse regenerative mode (Quadrant 2). The torque with negative speed became a bit smaller because the friction torque had changed direction.

Fig. 10(b) shows a 100 r/min step response with an 80% startup load step, fast ±100 r/min spin reversal and quadrant shift from forward motoring mode (Quadrant 1) to reverse regenerative mode (Quadrant 2). Again, torque at negative speed was a bit smaller than positive thanks to the assistance of friction torque.

Fig. 10(c) shows both 100 r/min step response, with a 50% load step applied at startup, and quadrant shift. With a step change of load direction, the motor then entered forward regenerative mode (Quadrant 4) via forward motoring mode (Quadrant 1).

Fig. 11(a) shows the 100 r/min step response under a 50% startup load step and robustness against large dc offset in current measurement. The +50% and +100% (of the amplitude of i_α and i_β) dc offset Δi_β was intentionally injected to i_β, leading to slight speed and position fluctuations.

Detection/correction mechanism verification was fulfilled by 100 r/min speed step responses under various unknown initial position offset/error scenarios, with a 50% startup load step and the exact command being forward motoring at 100 r/min.

1) Fig. 11(b) shows the actual rotor position was $\theta(0) = 0$, whereas $\hat{\theta}(0) = 90°$. The observed regeneration mode triggered correction, whose detection timeout was 920 ms.
2) Fig. 11(c) shows the actual rotor position was $\theta(0) = 0$, whereas $\hat{\theta}(0) = 180°$. The observed regeneration mode triggered correction, whose detection timeout was 920 ms.
3) Fig. 12(a) shows the actual rotor position was $\theta(0) = 90°$, whereas $\hat{\theta}(0) = 0$. The observed regeneration mode triggered correction, whose detection timeout was 920 ms.

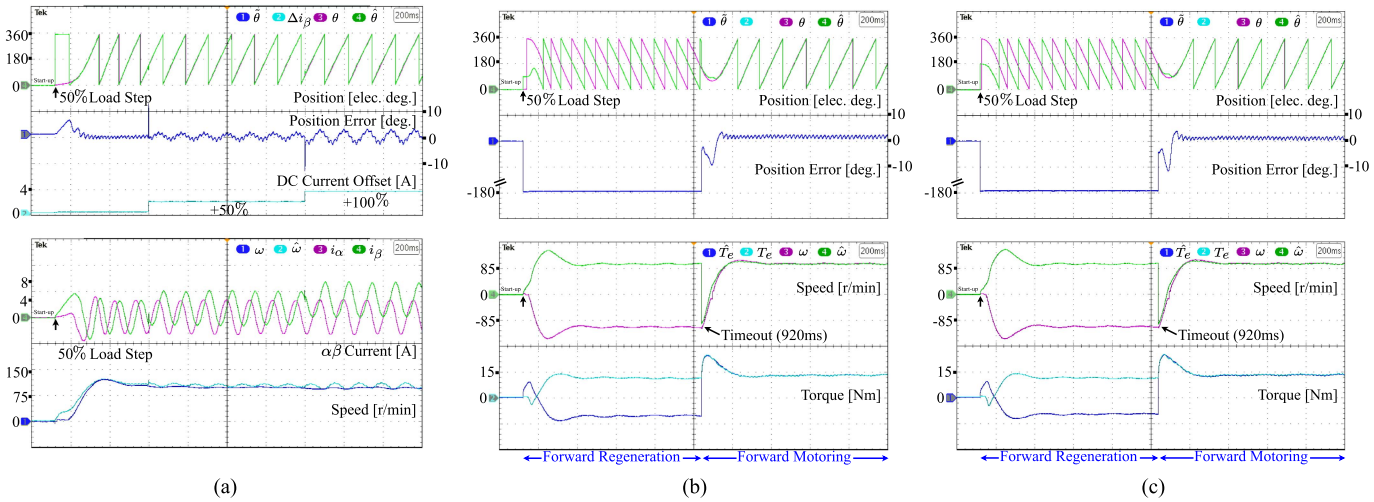

Fig. 11. (a) Speed step response of 100 r/min command and robustness, with a 50% startup load step and large $+50\%$ and $+100\%$ dc current offsets Δi_β added to the current measurement. (b) Speed step response at 100 r/min under 50% startup load. $\theta(0) = 0$ and $\hat{\theta}(0) = 90^\circ$ caused regeneration, a mismatch that activated correction at a preset 920 ms detection timeout. (c) Speed step response at 100 r/min under 50% startup load. $\theta(0) = 0$ and $\hat{\theta}(0) = 180^\circ$ caused regeneration, a mismatch that activated correction at a preset 920 ms detection timeout.

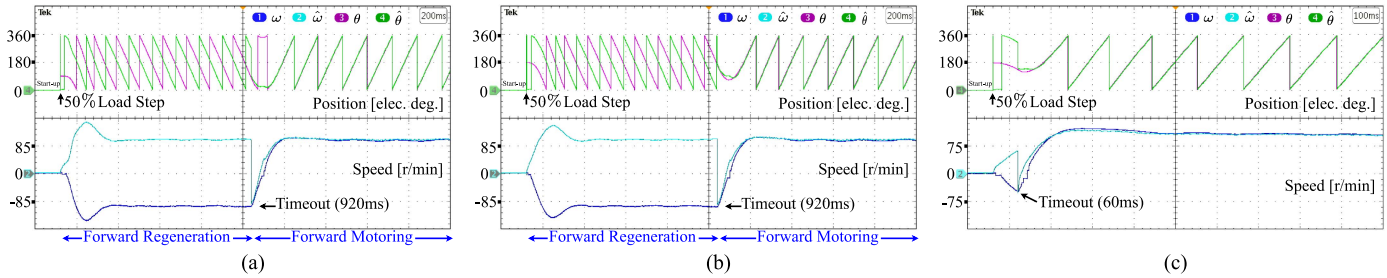

Fig. 12. (a) Speed step response at 100 r/min under 50% startup load. $\theta(0) = 90^\circ$ and $\hat{\theta}(0) = 0$ caused regeneration, a mismatch that activated correction at a preset 920 ms detection timeout. (b) Speed step response at 100 r/min under 50% startup load. $\theta(0) = 180^\circ$ and $\hat{\theta}(0) = 0$ caused regeneration, a mismatch that activated correction at a preset 920 ms detection timeout. (c) Speed step response at 100 r/min under 50% startup load. $\theta(0) = 180^\circ$ and $\hat{\theta}(0) = 0$ caused regeneration, a mismatch that activated correction at a preset 60 ms detection timeout.

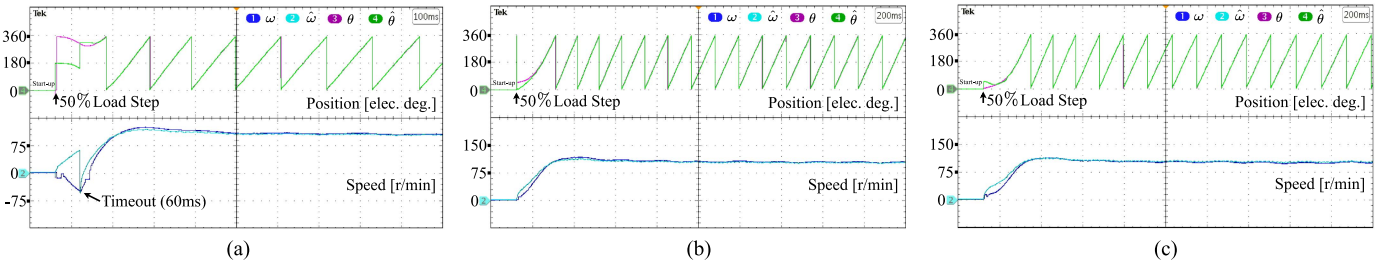

Fig. 13. (a) Speed step response at 100 r/min under 50% startup load. $\theta(0) = 0$ and $\hat{\theta}(0) = 180^\circ$ caused regeneration, a mismatch that activated correction at a preset 60 ms detection timeout. (b) Speed step response at 100 r/min under 50% startup load step. The initial error caused by $\theta(0) = 45^\circ$ and $\hat{\theta}(0) = 0$ was unable to activate correction at a preset detection timeout. (c) Speed step response at 100 r/min under 50% startup load step. The initial error caused by $\theta(0) = 0$ and $\hat{\theta}(0) = 45^\circ$ was unable to activate correction at a preset detection timeout.

4) Fig. 12(b) shows the actual rotor position was $\theta(0) = 180^\circ$, whereas $\hat{\theta}(0) = 0$. The observed regeneration mode triggered correction, whose detection timeout was 920 ms.
5) Fig. 12(c) shows the actual rotor position was $\theta(0) = 180^\circ$, whereas $\hat{\theta}(0) = 0$. The observed regeneration mode triggered correction, whose detection timeout was 60 ms.
6) Fig. 13(a) shows the actual rotor position was $\theta(0) = 0$, whereas $\hat{\theta}(0) = 180^\circ$. The observed regeneration mode triggered correction, whose detection timeout was 60 ms.

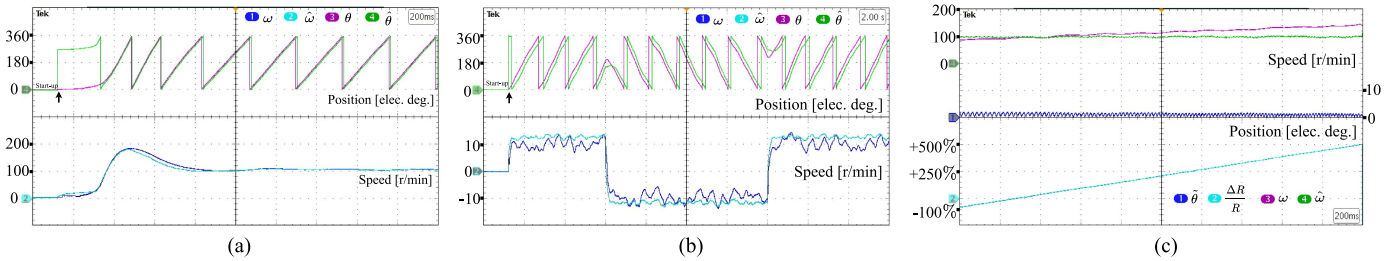

Fig. 14. (a) No load 100 r/min startup with $\theta(0) = 0$ and $\hat{\theta}(0) = -90°$, not triggering the correction. (b) Step responses of ± 10 r/min command without compensation for inverter irregularities. (c) Robustness test with $\Delta R/R$ varying from -100% to $+500\%$, 100 r/min and 50% load.

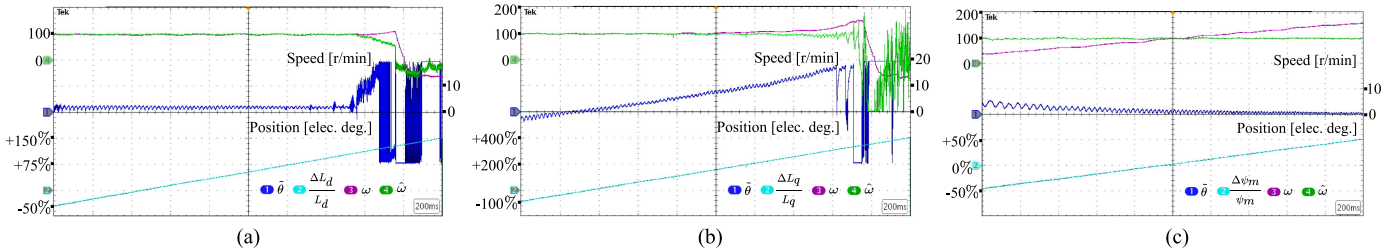

Fig. 15. (a) Robustness test with $\Delta L_d/L_d$ varying from -50% to $+150\%$, 100 r/min and 50% load. (b) Robustness test with $\Delta L_q/L_q$ varying from -100% to $+400\%$, 100 r/min and 50% load. (c) Robustness with $\Delta\psi_m/\psi_m$ varying from -50% to $+50\%$, 100 r/min and 50% load.

7) Fig. 13(b) shows the actual rotor position was $\theta(0) = 45°$, whereas $\hat{\theta}(0) = 0$, which was unable to trigger correction.
8) Fig. 13(c) shows the actual rotor position was $\theta(0) = 0$, whereas $\hat{\theta}(0) = 45°$, which could not trigger correction.

In Figs. 11(b)–12(b) the quit timeout was set to trigger at the steady-state and in the middle of the figures merely for a nice presentation. The timeout, as discussed in Section II-B, could be triggered as early as possible. For example, Figs. 12(c) and 13(a) show timeout was set to occur short after the startup.

Fig. 14(a) shows correction could not be triggered in 100 r/min no-load speed step response, with $\theta(0) = 0$ and $\hat{\theta}(0) = -90°$.

Fig. 14(b) shows ± 10 r/min, the lowest speed, fast spin reversal. To reproduce simulation feasibilities implied in, for example, Figs. 7(a)–(d), we recommend compensation.

Influence of the mismatched parameters was studied, and the maximum possible parameter mismatches that could cause the sensorless FOC system crash utterly were also explored.

Fig. 14(c) shows the test of robustness against ΔR, an extra error imposed to resistance R, carried out at 100 r/min with a 50% load. The value of $\Delta R/R$ varied from -100% to $+500\%$.

Fig. 15(a) shows the test of robustness against ΔL_d, an extra error imposed to inductance L_d, carried out at 100 r/min with a 50% load. The error $\Delta L_d/L_d$ varied from -50% to $+150\%$. It can be seen that the sensorless system crashed with $2L_d$.

Fig. 15(b) shows the test of robustness against ΔL_q, an extra error imposed to inductance L_q, carried out at 100 r/min with a 50% load. The error $\Delta L_q/L_q$ varied from -100% to $+400\%$. It can be seen that the sensorless system crashed with $3L_q$.

Fig. 15(c) shows the test of robustness against $\Delta\psi_m$, an extra error imposed to rotor flux ψ_m, carried out at 100 r/min with a 50% load. The error $\Delta\psi_m/\psi_m$ varied from -50% to $+50\%$. It can be seen that the speed estimate was sensitive to $\Delta\psi_m$.

IV. Conclusion

This article shows that the two familiar equations governing IPMSMs satisfy four (speed and position) pairs, which predicts sensorless algorithms end up in finite many ways and hence facilitate a primitive theoretic explanation of what may happen if sensorless IPMSMs startup with an unknown initial position. The proposed normal-reversal duality concept characterizes a normal state where the FOC system works fine with the real-world pair, and a reverse state where the FOC system manages imperfectly with a specious pair, as opposed to an utter crash. In case IPMSMs startup with an unknown initial position such that algorithms end up with a specious pair, a detection-quit mechanism using the knowledge of motor/generator mode is devised to help the FOC system be aware of and flee the erroneous reverse state the earlier the better.

An algorithm that preserves the IPMSM model intact and equipped with a quit mechanism is given. Evaluated according to seven necessary criteria of SOTAs and special startup tests tailored for unknown initial position scenarios, it exhibits effectiveness in both simulations and experiments. Experiments also reveal one severe disadvantage of this algorithm, that is, speed estimate is sensitive to the rotor flux parameter.

References

[1] Y. Sun, M. Preindl, S. Sirouspour, and A. Emadi, "Unified wide-speed sensorless scheme using nonlinear optimization for IPMSM drives," *IEEE Trans. Power Electron.*, vol. 32, no. 8, pp. 6308–6322, Aug. 2017.
[2] H. Li, Z. Wang, C. Wen, and X. Wang, "Sensorless control of surface-mounted permanent magnet synchronous motor drives using nonlinear optimization," *IEEE Trans. Power Electron.*, vol. 34, no. 9, pp. 8930–8943, Sep. 2019.
[3] R. Ortega, L. Praly, A. Astolfi, J. Lee, and K. Nam, "Estimation of rotor position and speed of permanent magnet synchronous motors with guaranteed stability," *IEEE Trans. Control Syst. Technol.*, vol. 19, no. 3, pp. 601–614, May 2011.

[4] P. Acarnley and J. Watson, "Review of position-sensorless operation of brushless permanent-magnet machines," *IEEE Trans. Ind. Electron.*, vol. 53, no. 2, pp. 352–362, Apr. 2006.
[5] G. Wang, M. Valla, and J. Solsona, "Position sensorless permanent magnet synchronous machine drives—A review," *IEEE Trans. Ind. Electron.*, vol. 67, no. 7, pp. 5830–5842, Jul. 2020.
[6] C. J. V. Filho, D. Xiao, R. P. Vieira, and A. Emadi, "Observers for high-speed sensorless PMSM drives: Design methods, tuning challenges and future trends," *IEEE Access*, vol. 9, pp. 56397–56415, 2021.
[7] A. Varatharajan, G. Pellegrino, E. Armando, and M. Hinkkanen, "Sensorless synchronous motor drives: A review of flux observer-based position estimation schemes using the projection vector framework," *IEEE Trans. Power Electron.*, vol. 36, no. 7, pp. 8171–8180, Jul. 2021.
[8] H. Wang, Y. Yang, X. Ge, Y. Zuo, Y. Yue, and S. Li, "PLL- and FLL-based speed estimation schemes for speed-sensorless control of induction motor drives: Review and new attempts," *IEEE Trans. Power Electron.*, vol. 37, no. 3, pp. 3334–3356, Mar. 2022.
[9] Z. Zhang, "Sensorless back EMF based control of synchronous PM and reluctance motor drives—A review," *IEEE Trans. Power Electron.*, vol. 37, no. 9, pp. 10290–10305, Sep. 2022.
[10] J. Chen, X. Yuan, F. Blaabjerg, and C. H. T. Lee, "Overview of fundamental frequency sensorless algorithms for AC motors: A unified perspective," *IEEE Trans. Emerg. Sel. Topics Power Electron.*, vol. 11, no. 1, pp. 915–931, Feb. 2023.
[11] *InstaSPIN-FOC and InstaSPIN-MOTION User's Guide (Rev. I)*. Dallas, Tx, USA: Texas Instruments, Oct. 2021.
[12] *The Sensorless Servo FR-E720EX & MM-GKR Series*. Tokyo, Japan: Mitsubishi Electric, Jan. 2015.
[13] "Sensorless motor control & digital power with STM32," STMicroelectronics, Oct. 2023.
[14] I. Boldea, M. C. Paicu, and G.-D. Andreescu, "Active flux concept for motion-sensorless unified AC drives," *IEEE Trans. Power Electron.*, vol. 23, no. 5, pp. 2612–2618, Sep. 2008.
[15] G. Foo and M. Rahman, "Sensorless direct torque and flux-controlled IPM synchronous motor drive at very low speed without signal injection," *IEEE Trans. Ind. Electron.*, vol. 57, no. 1, pp. 395–403, Jan. 2010.
[16] Q. Lin, L. Liu, and D. Liang, "Adaptive observer design for sensorless IPMSM drives with known regressors variant of extended EMF model," *IEEE Trans. Power Electron.*, vol. 39, no. 1, pp. 212–224, Jan. 2024.
[17] S. Zhou et al., "A robust encoderless control for PMSM drives: A revised hybrid active flux-based technique," *IEEE Trans. Power Electron.*, vol. 38, no. 11, pp. 14438–14449, Nov. 2023.
[18] M. X. Bui, D. Guan, D. Xiao, and M. F. Rahman, "A modified sensorless control scheme for interior permanent magnet synchronous motor over zero to rated speed range using current derivative measurements," *IEEE Trans. Ind. Electron.*, vol. 66, no. 1, pp. 102–113, Jan. 2019.
[19] Q. Dong, B. Wang, Y. Yu, M. Tian, and D. Xu, "A rotor position estimation scheme using inherent excitation source for finite-control set model predictive control in low-speed region," *IEEE Trans. Ind. Electron.*, early access, Apr. 29, 2024, doi: 10.1109/TIE.2024.3384580.
[20] H. Li, B. Nahid-Mobarakeh, and A. Emadi, "Global observability of sensorless IPMSMs," *IEEE Trans. Autom. Control*, vol. 69, no. 5, pp. 3365–3372, May 2024.

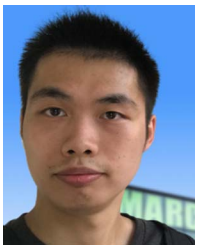

Haomin Li received the B.S. and M.S. degrees in electrical engineering from Southeast University, Nanjing, China, in 2016 and 2019, respectively. He is currently working toward the Ph.D. degree in electrical and computer engineering with McMaster University, Hamilton, ON, Canada.

His research interests include sensorless permanent magnet synchronous motor drives.

Babak Nahid-Mobarakeh (Fellow, IEEE) received the Ph.D. degree in electrical engineering from the Institut National Polytechnique de Lorraine, Nancy, France, in 2001.

From 2001 to 2006, he was with the Centre de Robotique, Electrotechnique et Automatique, University of Picardie, Amiens, France. In 2006, he joined the Ecole Nationale Superieured'Electricite et de Mecanique, University of Lorraine, Nancy, where he was a Professor until 2019. Since 2020, he has been a Professor at McMaster University, ECE Dept., Hamilton, ON, Canada. He has authored or coauthored more than 300 international peer-reviewed journal and conference papers as well as several book chapters. He also holds six published patents. His research interests include nonlinear and robust control design for power converters and motor drives, fault detection and fault-tolerant control of electric systems, and design, control, and stabilization of microgrids.

Dr. Nahid-Mobarakeh was the recipient of several IEEE awards. He was the General Chair of the 2020 IEEE Transportation Electrification Conference and Expo. Between 2012 and 2019, he was an Officer and then the Chair of the Industrial Automation and Control Committee (IACC), IEEE Industry Applications Society (IAS). He was also the IACC Committee Administrator and a Technical Committee Paper Review Chair for IEEE TRANSACTIONS ON INDUSTRY APPLICATIONS. Currently, he is the vice-chair of the IEEE Power Electronics Society Technical Committee on Electrified Transportation Systems. He is also a Member of the Power Electronics and Motion Control Council.

Ali Emadi (Fellow, IEEE) received the B.S. and M.S. degrees in electrical engineering with highest distinction from the Sharif University of Technology, Tehran, Iran, in 1995 and 1997, respectively, and the Ph.D. degree in electrical engineering from Texas A&M University, College Station, TX, USA, in 2000.

He is the Canada Excellence Research Chair Laureate with McMaster University, Hamilton, ON, Canada. He is also the holder of the NSERC/FCA Industrial Research Chair in Electrified Powertrains and Tier I Canada Research Chair in Transportation Electrification and Smart Mobility. Before joining McMaster University, he was the Harris Perlstein Endowed Chair Professor of Engineering and Director of the Electric Power and Power Electronics Center and Grainger Laboratories at Illinois Institute of Technology, Chicago, IL, USA, where he established research and teaching facilities as well as courses in power electronics, motor drives, and vehicular power systems. He was the Founder, Chair of the Board of Directors, and President of Hybrid Electric Vehicle Technologies, Inc. (HEVT) — a university spin-off company of Illinois Tech. Currently, he is the Founder, President, and Chief Executive Officer of Enedym Inc. and Founder and Chair of the Board of Directors of Menlolab Inc.—two McMaster University spin-off companies. He has authored or coauthored more than 700 journal and conference papers as well as several books including Vehicular Electric Power Systems (2003), Energy Efficient Electric Motors (2004), Uninterruptible Power Supplies and Active Filters (2004), Modern Electric, Hybrid Electric, and Fuel Cell Vehicles (2nd ed, 2009), and Integrated Power Electronic Converters and Digital Control (2009). He is also the editor of the Handbook of Automotive Power Electronics and Motor Drives (2005) and Advanced Electric Drive Vehicles (2014). He is the coeditor of the Switched Reluctance Motor Drives (2018).

Dr. Emadi was the Inaugural General Chair of the 2012 IEEE Transportation Electrification Conference and Expo (ITEC) and has chaired several IEEE and SAE conferences in the areas of vehicle power and propulsion. He was the founding Editor-in-Chief of IEEE TRANSACTIONS ON TRANSPORTATION ELECTRIFICATION from 2014 to 2020.